# Overcoming the challenges of a shallow-water sparse wide-azimuth survey to improve deep reservoir imaging in the East China Sea

Yun Wei[1], Hua Chen[1], Senqing Hu[1], Peipei Deng[2], Yongdeng Xiao[2], Srujan Poonamalli[2], Robert To[2], Joe Zhou[2], Jason Sun[2], Gang Yao[1], and Yu Jiang[1]

https://doi.org/10.1190/tle38080610.1.

## Abstract

A new broadband wide-azimuth towed-streamer (WATS) survey was acquired to better resolve reservoir compartments in a shallow-water region of the East China Sea. To offset the shortcomings of narrow-azimuth acquisition along the strike direction, two vessels were added side-by-side as additional source vessels to form the WATS acquisition geometry for this survey. This WATS acquisition was much sparser than typical WATS surveys used in deepwater environments due to its one-sided configuration. The combination of sparse acquisition, shallow water, and deep targets set the challenge of how to optimally reveal the potential of side-gun data to improve the final image. Three-dimensional effects and severe aliasing in the crossline direction pose significant challenges for side-gun data processing. We present a comprehensive workflow to resolve these challenges consisting of 3D deghosting, 3D model-based water-layer demultiple, 3D surface-related multiple elimination, and 4D regularization for sparse and shallow-water wide-azimuth data. A tilted orthorhombic velocity model is built with better constraints from the wide-azimuth data, leading to improved fault positioning and imaging. Side-gun data clearly enhance the final target reservoir image and tie better with well data due to improved illumination. A new channel is discovered based on interpretation from the inverted $V_P/V_S$, explaining the previous incorrect prediction for one failed well that was drilled into a thinner and shallower channel unconnected to the main reservoir. An analysis of the impact of side-gun data from different offsets and azimuths shows that better azimuthal distribution within middle offset ranges had a more significant impact than far offsets in the final image of this survey. This information provides valuable reference in similar geologic conditions for future acquisition designs.

## Introduction

The study area is located in a shallow-water region of the East China Sea with a water bottom around 70–100 m in depth. The production field has several wells drilled into the target reservoir. One was a failed well, while the rest were all successful and drilled into the production field. The legacy seismic image indicates that all of the wells, including the failed one, should have been drilled into the same structure between 3.1 and 3.6 km in depth. Therefore, it was concluded that the legacy data were inadequate for resolving reservoir compartments. New broadband data with good low-frequency signals were preferred (Chen et al., 2017). Legacy acquisition followed the dip direction, but the new acquisition had to follow the strike direction due to operational limitations as shown in Figure 1a. Meanwhile, 3D effects of the structure favor more azimuthal information. To overcome this limitation, two vessels were added side-by-side as additional source vessels on one side of the streamer vessel to form the wide-azimuth towed-streamer (WATS) acquisition geometry. The side guns provided the required reflection information in the dip direction.

The WATS acquisition setup consisted of three vessels and four guns shooting in sequence, as shown in Figure 1b, with the acquisition carried out in two passes. The streamer boat had two guns and 10 cables with a 100 m cable separation and 6 km cable length. The shot geometry had a 50 m interval between the two guns and a 50 m interval between shot points from the same gun. The cable profile was slanted for ghost notch diversity and broader bandwidth with depth varying from 7 m at near offsets to 40 m at far offsets. The side vessels each had one gun and were positioned laterally at a distance of 1 and 2 km from the streamer vessel centerline for the first pass and at a distance of 3 and 4 km for the second pass. The streamer vessel centerline shifted 12.5 m along the crossline direction during the second pass to improve subsurface coverage. Rather than at the center of the cable where the vessel would be within 10° of the nearest cable feathering range, as shown in Figure 1b, the inner side vessel was located 2 km behind the first channel in the inline direction in order to avoid potential entanglement from cable feathering. The outer side vessel was located 3 km behind the first channel. Figure 1c shows the azimuth and offset distribution of this acquisition geometry.

Relative to typical WATS surveys in deepwater environments such as the Gulf of Mexico (Michell et al., 2006), the new acquisition was sparser for the following two reasons. Only one streamer vessel was deployed in the acquisition, and the side vessels were positioned on only one side of the streamer vessel. With such sparsity of the wide-azimuth acquisition in a shallow-water environment, the key challenge is how to leverage the full potential of the additional source vessels by data processing. Among the many challenges that must be overcome are deghosting, demultiple, regularization, and anisotropic velocity model building. In the following sections, we discuss these challenges and demonstrate the full advantages of this new WATS acquisition.

[1]CNOOC Shanghai, Shanghai, China. E-mail: weiyun@cnooc.com.cn; chenhua@cnooc.com.cn; husq@cnooc.com.cn; yaogang2@cnooc.com.cn; jiangyu@cnooc.com.cn.
[2]CGG, Singapore. E-mail: peipei.deng@cgg.com; yongdeng.xiao@cgg.com; srujan.poonamalli@cgg.com; robert.to@cgg.com; joe.zhou@cgg.com; jason.sun@cgg.com.

## Deghosting

Three-dimensional deghosting for side-gun data is not a new topic, especially in deepwater regions (Wang et al., 2014; Wu et al., 2014). The severe aliasing expected in the crossline direction and 3D effects must be addressed for the side-gun data, while shallow-water environments pose additional challenges and issues. The *p* estimations of the shallow primary reflection energy may be inaccurate due to strong refraction energy arriving early and masking the shallow primary reflection energy. The apparent velocity of the strong refraction energy varies between shots from different side guns. Therefore, accurate 3D linear noise attenuation (LNA) is critical for effective deghosting. Figure 2a shows a shot gather after 2.5 Hz low-cut filtering. Strong refraction linear noise masks the shallow primary reflection events. A progressive sparse tau-p transformation starting from low frequencies (Wang and Nimsaila, 2014) provides a feasible solution for removing the strong aliased noise. Figure 2b shows the shot gather after 3D LNA. Figures 2c and 2d show the same shot gather after 2D and 3D deghosting, respectively. Two-dimensional deghosting introduced ringing and left a substantial amount of residual ghost energy in the data due to strong 3D effects. Three-dimensional deghosting effectively removed the ghost energy and revealed underlying multiples. The autocorrelation shows the underlying multiples as relatively flat trough energy. In addition to the early arrival of strong refraction energy, the receiver-side ghost notch frequency and the shallow-water multiple notch frequency may coincide with each other in certain areas on far channels. These channels require extra attention in the deghosting and demultiple stages.

## Demultiple

Relative to narrow-azimuth towed-streamer (NATS) data, WATS data are known to better stack out multiples (VerWest and Lin, 2007). This suppression phenomenon comes from the higher fold of the mid- to far-offset traces, as the offset increment is no longer constant in the WATS data. The nonzero slope of

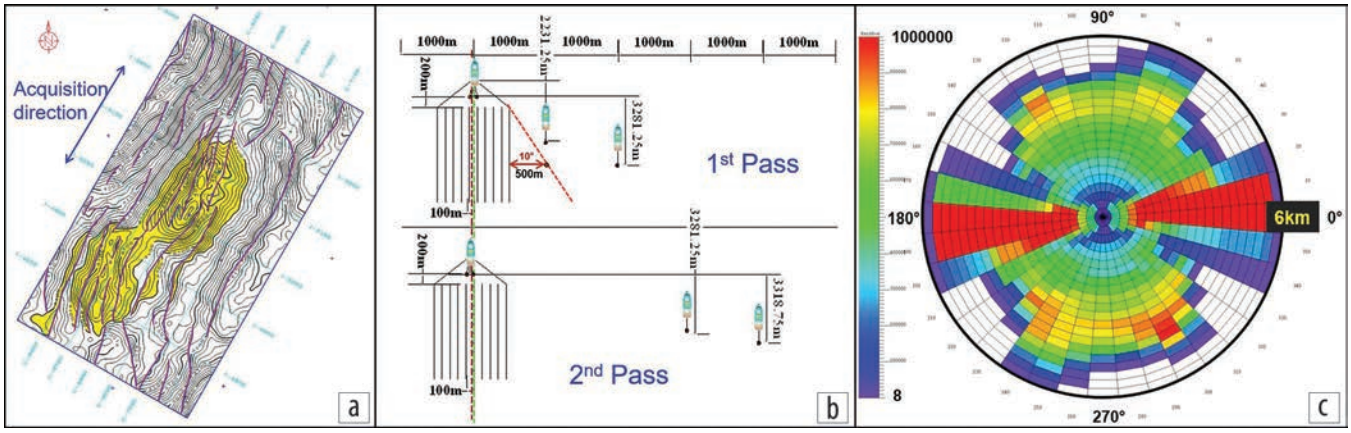


**Figure 1.** (a) Survey map. (b) WATS acquisition geometry. (c) Corresponding rose diagram.

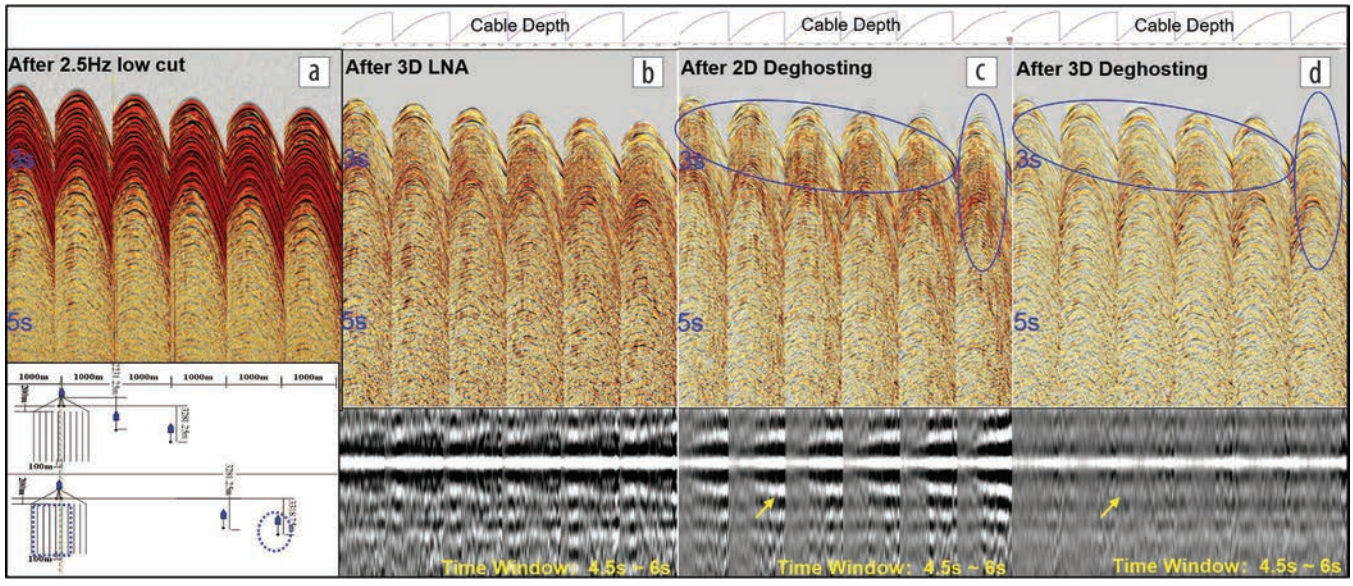


**Figure 2.** Side-gun shot gathers and corresponding autocorrelations (a) after 2.5 Hz low-cut filtering, (b) after 3D LNA with strong shallow refraction energy attenuated, (c) after 2D deghosting, and (d) after 3D deghosting. The blue ovals in (c) indicate areas with ringing introduced by 2D deghosting, which becomes worse moving toward outer cables with stronger 3D effects. The yellow arrow points to the ringing and residual ghost energy on the autocorrelation. After 3D deghosting, the ringing is not present on the shot gather or autocorrelation in (d), and residual ghost energy is much less than the 2D results.

the multiples at near offsets ensures better cancellation in that range than the NATS case. Figure 3a shows a NATS common-midpoint (CMP) gather with a conventional parabolic multiple moveout. The multiples in the WATS CMP gather shown in Figure 3b have a more linear moveout with much steeper dipping angle with offset. Figure 3c shows the corresponding offset histogram from the WATS CMP gather.

However, the water bottom is so shallow in this region that multiple and primary moveout overlap each other, and whether the multiple suppression phenomenon is still obvious becomes a natural question. Figure 4 shows a comparison of the main gun, main gun and first-pass side gun, and main gun and all side-gun stacks from the WATS data after deghosting. The NATS stack containing only main-gun data shows clear water-layer-related first-bounce multiples on the autocorrelation. By adding the first-pass side-gun data to the stack, a clear suppression of the first-bounce multiple energy was observed. When all guns contributed to the stack, the multiple energy was further attenuated.

Despite the natural multiple suppression capability of sparse WATS data for this shallow-water case, an effective demultiple processing flow was still critical for removing residual multiple energy and improving the final gather quality. For this survey, 3D model-based water-layer demultiple (MWD) was applied for

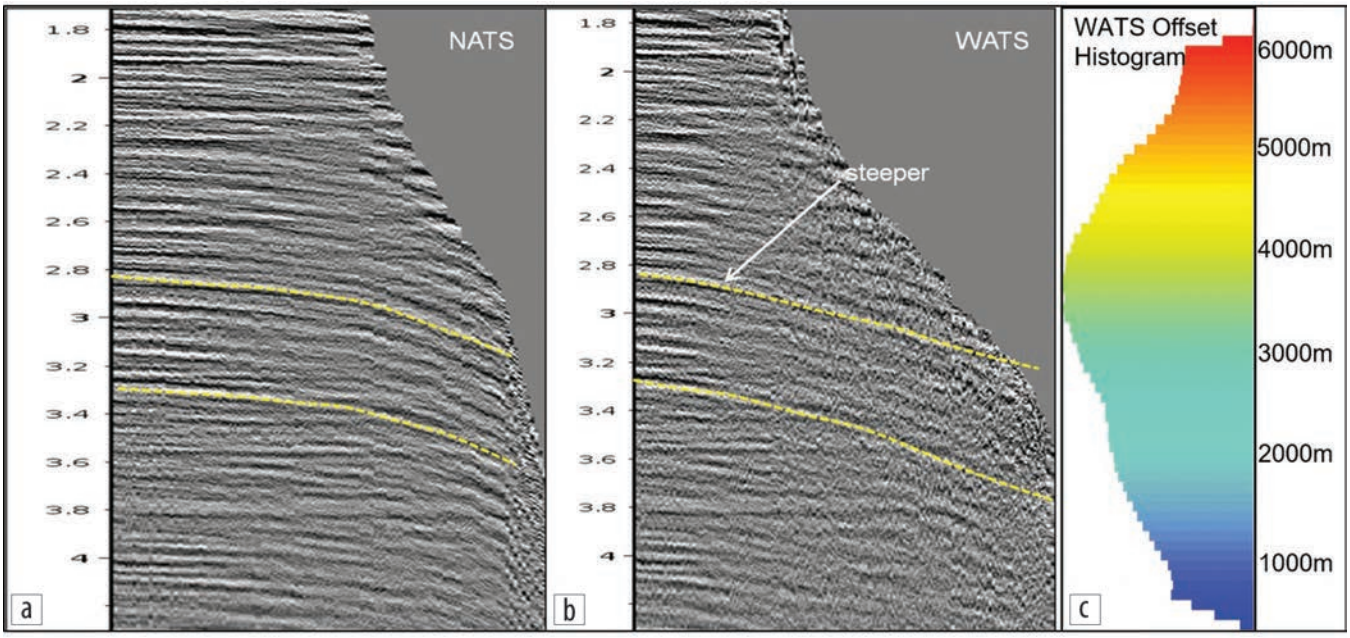


**Figure 3.** (a) NATS CMP gather with approximate parabolic multiple moveout. (b) WATS CMP gather with more linear multiple moveout. (c) WATS data offset histogram showing higher fold at middle and far offsets.

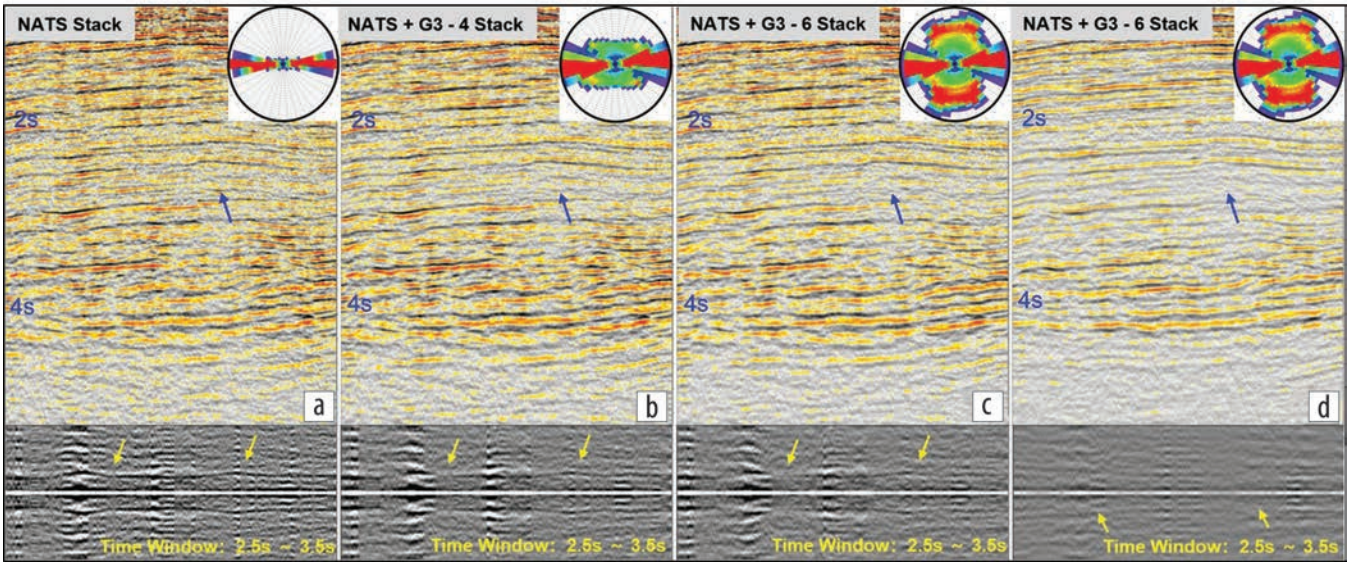


**Figure 4.** Stacks after deghosting for (a) NATS with only main-gun data, (b) NATS plus first-pass side-gun data, and (c) NATS plus all side-gun data. (d) Stack after deghosting and demultiple for NATS plus all side-gun data. The corresponding autocorrelations are shown below each stack.

cases where the water bottom reflection was poorly recorded, while longer period multiples were targeted with 3D surface-related multiple elimination (SRME). Figures 4c and 4d show the full stack before and after the proposed demultiple flow. Figure 4d shows that the residual multiple energy was greatly reduced.

## 4D regularization and interpolation

Regularization is an important step for ray-tracing-based migrations. For conventional narrow-azimuth data, migration swings due to insufficient regularization are less obvious. However, for sparse WATS data, as the crossline offset variation is quite large within one common-offset vector, it is impossible to compensate for the offset variation through a simple partial normal moveout correction. The variation is even worse for residual multiple energy in shallow-water environments. Such variations will generate strong swings on the migrated image. Figure 5a shows the common-offset prestack depth migration (PSDM) image with strong migration swings from 3D regularization and interpolation where the offset dimension variations were not properly taken into account.

In 4D regularization, a Fourier transform is applied to the offset dimension and regularized in the frequency domain (Wang and Wang, 2014). This procedure better honors the moveout, including anisotropic moveout, for all sorts of energy and is a necessary step for reducing noise on the image. Figure 5b shows a much improved common-offset image generated from the same input data as Figure 5a but with 4D regularization and interpolation. The higher signal-to-noise ratio (S/N) is noticeable on the offset gathers. The quality of this data is key to a successful $V_P/V_S$ inversion, as the S/N has a direct impact on the offset gather amplitude fidelity determining the amplitude-variation-with-offset analysis and the $V_P/V_S$ inversion.

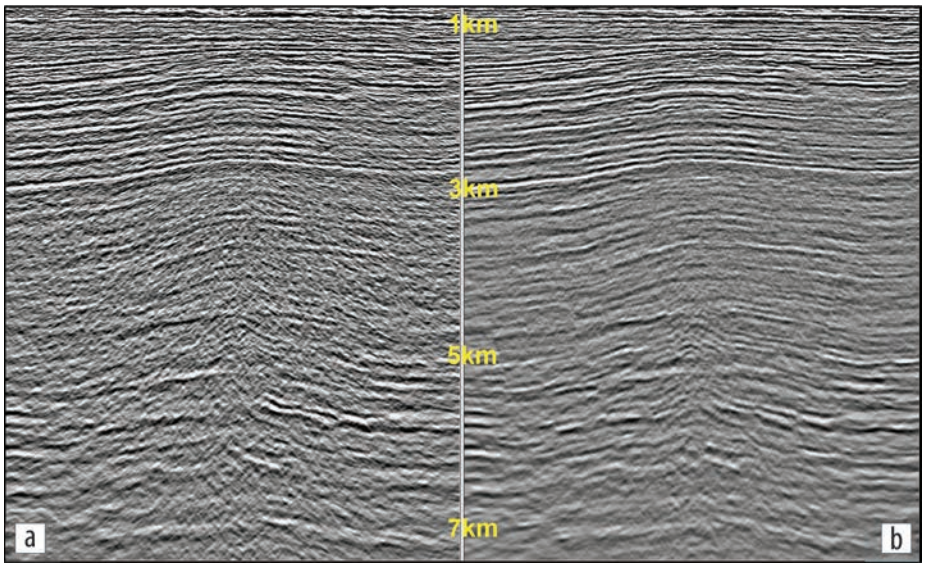


**Figure 5.** Common-offset PSDM image (offset X = 525 m, offset Y = 1000 m) from (a) 3D regularization and interpolation and (b) 4D regularization and interpolation. With 4D regularization and interpolation, the image is much cleaner.

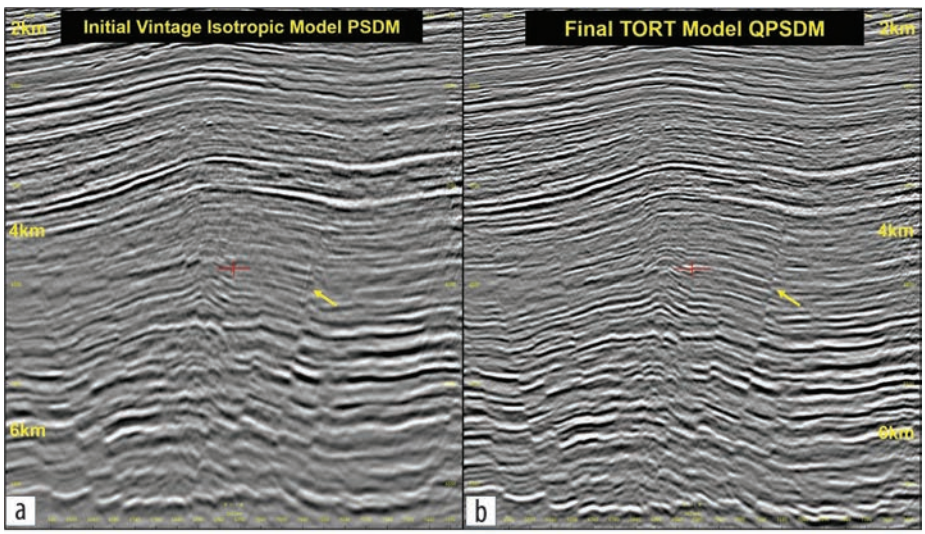


**Figure 6.** (a) Initial vintage isotropic model PSDM image. (b) Final TORT model QPSDM image. The yellow arrows point to the faults with obvious uplift from a better anisotropic velocity model compared to the vintage model.

## Velocity model update

While wide-azimuth data require more attention at the regularization stage, they also provide additional azimuthal and spatial constraints for velocity updates (Zhou et al., 2015). Diving-wave full-waveform inversion (FWI) was performed to update the velocity in the shallow section down to 1.5 km. The data were split into individual azimuth sectors, and ray-based tomography was applied in addition to diving-wave FWI to update the velocity model of each individual sector. The tomography updated the velocity in the deep target zone from 3 to 5 km. An orthorhombic velocity model was then constructed from the individual azimuth sector velocity models. Fault imaging and positioning were greatly improved since the orthorhombic model ensured better consistency between images from different azimuthal data. Despite the weak azimuthal anisotropy observed in the survey area, the image still benefits from the anisotropic model update. A background $Q$ model was also included using central-frequency shift $Q$ tomography to compensate for attenuation (Hung et al., 2015).

Figure 6a shows the initial vintage velocity model PSDM image where the fault imaging in the target zone is smeared, and the resolution is

inadequate for the subsequent interpretation work. Figure 6b shows the final tilted orthorhombic (TORT) *Q* prestack depth migration (QPSDM) image with improved fault positioning and imaging. Seismic resolution at the reservoir area is also much higher due to a combination of broader bandwidth from acquisition, deghosting, and better *Q* compensation.

## Side-gun data analysis

Wide-azimuth data are known to provide better illumination and more undershoot rays to enhance the imaging quality in areas of complex geology. After resolving the migration input challenges and building an orthorhombic velocity model, a comparison was made to analyze the impact of side-gun data to the final image.

Figure 7 shows a comparison of the extracted root-mean-square (rms) amplitude map from the target horizon at around a 3.5 km depth from different stack volumes. Figures 7a and 7d are from the NATS case using only main-gun data, while Figures 7b and 7e and Figures 7c and 7f further include the first-pass side-gun data and both passes of side-gun data, respectively. The first-pass side gun has a dramatic impact on the final reservoir structural imaging and on the improvement of S/N, while the impact of the second-pass side gun is less striking. These analyses all show substantial uplift from the first-pass side-gun data and less significant impact from the second pass. In general, side-gun data provide more spatial constraints for more reliable velocity updates. However, the impact on velocity updates from the second pass was limited due to the very weak azimuthal anisotropy in this region. This analysis provided valuable guidance for future survey designs in similar geologic settings. For instance, instead of farther away for longer offset distribution, one could consider placing the second-pass side gun closer to the streamer center line for better azimuth distribution.

## Results

The WATS final QPSDM image has increased S/N, broadened bandwidth, and improved fault imaging relative to the legacy image (Figures 8a and 8b). Elastic rock property inversion results also show obvious improvements from the new WATS broadband QPSDM data in addition to the enhanced final image.

The final result benefits from both the wide-azimuth acquisition and targeted broadband wide-azimuth processing technology that better utilized the newly acquired data. Figure 8c shows a clear channel system interpretation on the new WATS QPSDM image, which is not clear on the legacy prestack time migration

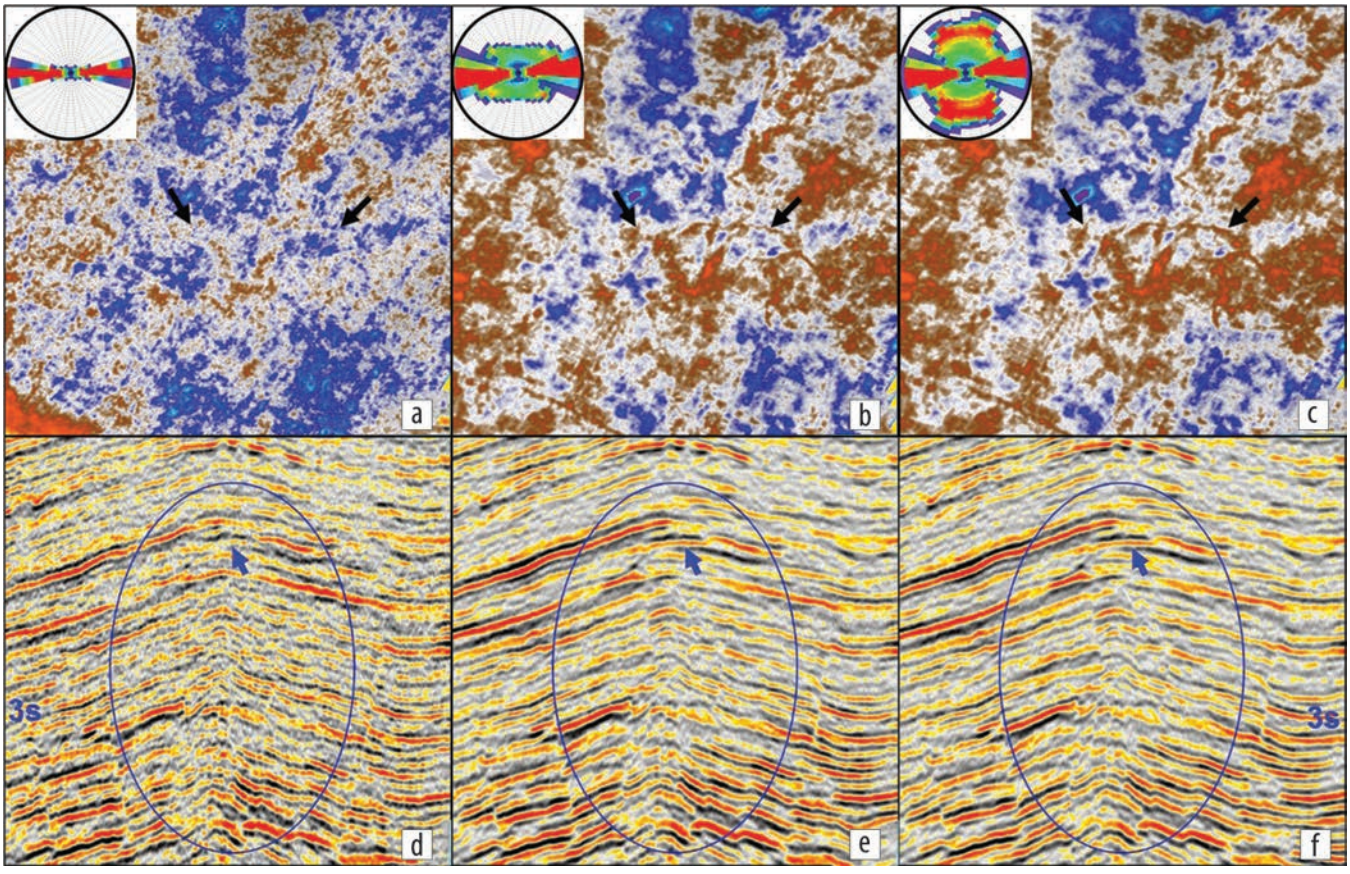


**Figure 7.** Impact of side guns on rms amplitude maps at a target reservoir horizon (a–c) taken from PSDM stacks (d) and (f). (a) and (d) NATS only. The black arrow on the rms map points to a structural feature that is not clear from the NATS data. A similar observation is made on the PSDM stack indicated by the blue arrow. The blue oval circles the target fault imaging with obvious noise. (b) and (e) NATS plus first-pass side-gun data. The structural feature is more prominent on the rms map (black arrow) and on the PSDM stack (blue arrow). The fault imaging is much clearer (blue oval). (c) and (f) NATS plus two passes of side-gun data. The coherency of the PSDM stack is improved, but the uplift of the structural features and fault imaging when adding the second-pass data is less striking.

(PSTM) image (Figure 8d). Figure 8e shows the legacy inverted $V_P/V_S$, which predicts the one failed well on the same channel system as a successful well. The $V_P/V_S$ inverted from the WATS QPSDM data allows for interpretation of a new channel, explaining the observations from the failed well (Figures 8f and 8g).

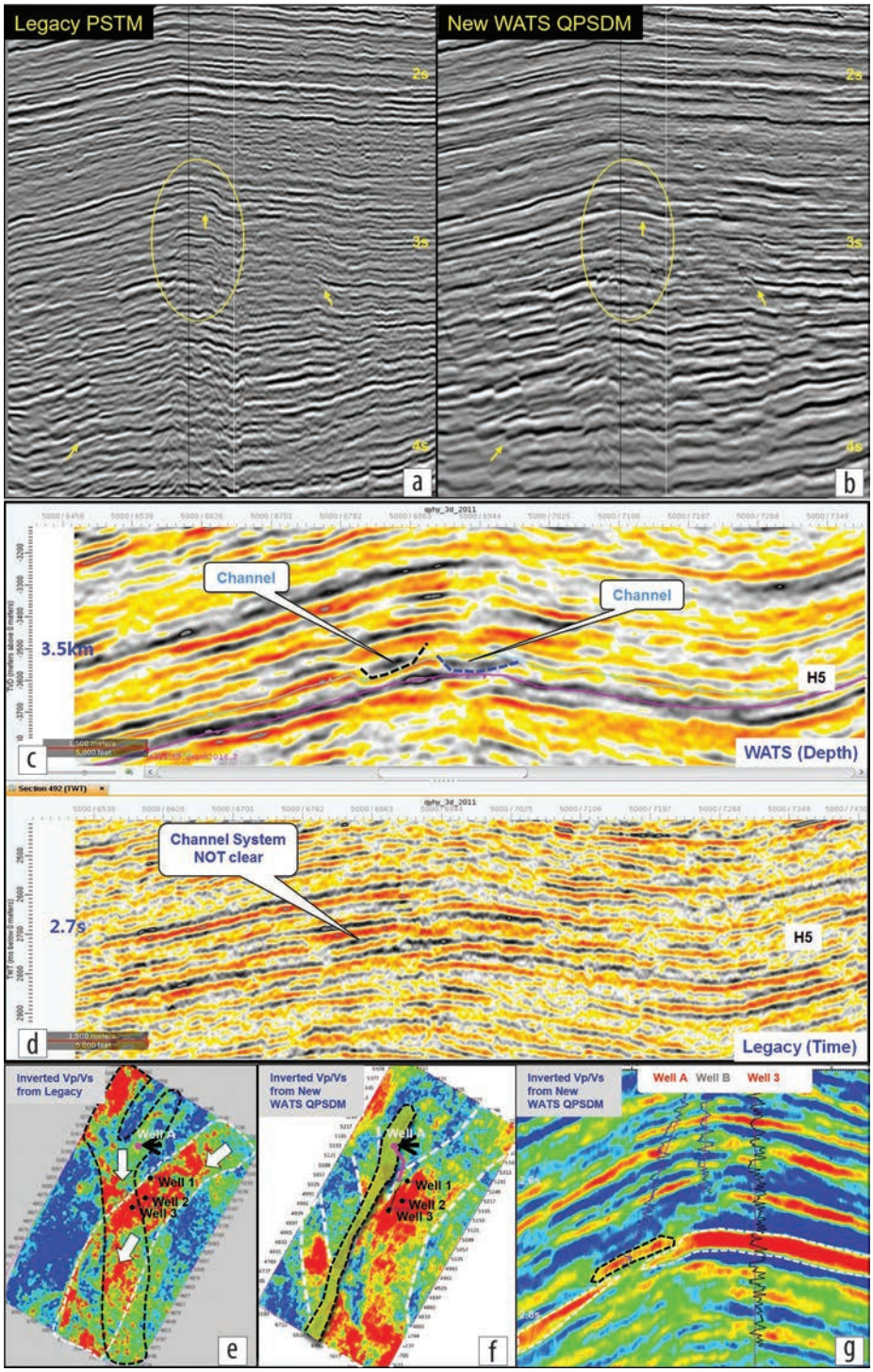


**Figure 8.** (a) Legacy PSTM stack in time. (b) New WATS QPSDM stack in time. (c) Channel interpretation on the new WATS QPSDM image. (d) Legacy PSTM image with no clear indication of the channel system. (e) Inverted $V_P/V_S$ from legacy data at the target reservoir with interpretation of two large channels defined by black and white dashed lines. (f) Inverted $V_P/V_S$ from the new WATS QPSDM data at the target reservoir with interpretation of one large channel defined by white dashed lines and one shallower and thinner channel defined by black dashed lines with the failed production well (black arrow). (g) Vertical section from the inverted $V_P/V_S$ from the new WATS QPSDM data shows the shallower channel (black dashed lines) not connected to the main channel beneath (white dashed lines).

## Conclusion

A combination of broadband WATS acquisition and advanced data processing workflows successfully resolved the deep target imaging challenges in a shallow-water environment. Three-dimensional LNA and 3D deghosting using a progressive sparse tau-p transformation on the side-gun data were critical for removing ghost energy. Although wide-azimuth data sets can improve multiple attenuation through stacking, 3D MWD and 3D SRME were needed to further remove multiple energy and improve the final image quality. Regularization and interpolation in 4D can effectively transform and regularize the data in the additional offset dimension, reducing migration swings. Azimuthal anisotropy variations seen in the WATS data were incorporated in the TORT model building for better fault positioning and imaging. Elastic rock property inversion based on the new data explained the failed well and improved understanding of the reservoir compartments. Detailed contribution analysis indicated that the second-pass side vessels can be placed closer to the streamer vessel to improve azimuth distribution, which is a valuable reference for future survey designs. TLE


## Acknowledgments

The authors thank CGG and CNOOC for permission to publish this work. They also thank Yunxin Mao from CNOOC for his inversion work.


## Data and materials availability

Data associated with this research are confidential and cannot be released.


Corresponding author: peipei.deng@cgg.com


## References


Chen, H., S. Hu, Y. Wei, P. Deng, Y. Xiao, W. Kuang, S. Cao et al., 2017, Improved deep target reservoir imaging with broadband WATS data in the East China Sea: 79th Conference and Exhibition, EAGE, Extended Abstracts, https://doi.org/10.3997/2214-4609.201701140.

Hung, B., X. Wang, Y. P. Phan, R. Alai, K. Xin, Y. He, N. N. Rahman, and

W. H. Tang, 2015, Full broadband processing including total *Q* compensation in the presence of gas: 85th Annual International Meeting, SEG, Expanded Abstracts, 4080–4084, https://doi.org/10.1190/segam2015-5936968.1.

Michell, S., E. Shoshitaishvili, D. Chergotis, J. Sharp, and J. Etgen, 2006, Wide azimuth streamer imaging of Mad Dog; Have we solved the subsalt imaging problem?: 76th Annual International Meeting, SEG, Expanded Abstracts, 2905–2909, https://doi.org/10.1190/1.2370130.

VerWest, B. J., and D. Lin, 2007, Modeling the impact of wide-azimuth acquisition on subsalt imaging: Geophysics, **72**, no. 5, SM241–SM250, https://doi.org/10.1190/1.2736516.

Wang, J., and S. Wang, 2014, Anisotropy-preserving 5D interpolation by hybrid Fourier transform: Presented at GeoConvention: FOCUS, CSEG.

Wang, P., and K. Nimsaila, 2014, Fast progressive sparse tau-p transform for regularization of spatially aliased seismic data: 84th Annual International Meeting, SEG, Expanded Abstracts, 3589–3593, https://doi.org/10.1190/segam2014-0889.1.

Wang, P., S. Ray, and K. Nimsaila, 2014, 3D joint deghosting and crossline interpolation for marine single-component streamer data: 84th Annual International Meeting, SEG, Expanded Abstracts, 3594–3598, https://doi.org/10.1190/segam2014-0882.1.

Wu, Q., C.-C. Lee, W. Zhao, P. Wang, and Y. Li, 2014, 3D deghosting for full-azimuth and ultra-long offset marine data: 84th Annual International Meeting, SEG, Expanded Abstracts, 4238–4242, https://doi.org/10.1190/segam2014-1297.1.

Zhou, B., J. Zhou, L. Liu, F. C. Loh, J. Liu, Y. Xie, Z. Wang, and X. Pu, 2015, Orthorhombic velocity model building and imaging of Luda Field with WAZ OBC data: 85th Annual International Meeting, SEG, Expanded Abstracts, 5212–5216, https://doi.org/10.1190/segam2015-5879535.1.